Paul, J.D.H.; Hoppe, R.; Appel, F.:
On the Bauschinger Effect in TiAl Alloys
In: Acta Materialia (2015) Elsevier

DOI: 10.1016/j.actamat.2015.10.036

On the Bauschinger Effect in TiAl Alloys

Jonathan D.H. Paul, Roland Hoppe and Fritz Appel*

Institute for Materials Research, Helmholtz-Zentrum Geesthacht,

D-21502 Geesthacht, Germany

*corresponding author

Abstract

The Bauschinger effect has been investigated at room temperature on a multiphase titanium aluminide alloy based on γ(TiAl). The effect of strain reversal was assessed by comparing uni-directional tensile tests with those performed on specimens made from pre-compressed material. This deformation sequence has the advantage that both the forward and reverse parts of the Bauschinger cycle are in tension, i.e., they are not affected by non-axial deformation, buckling or specimen end constraint. The results suggest that no permanent softening develops upon strain reversal whereas significant transient softening is present. The effect seems to be caused by heterogeneities in the deformed state due to the multiphase constitution of the material.

Keywords: Titanium aluminides; Bauschinger effect; Strain gradients; Internal stresses; Strain rate sensitivity

1. Introduction

The Bauschinger effect, first reported in 1886 [1], is primarily concerned with a reduction of yield stress upon load reversal. The phenomenon is usually associated with directional internal back stresses that develop during work hardening. On reversing the straining direction, the back stresses produced during prior loading are thought to be in the same direction as the applied shear stress. Thus, dislocation motion in the reversed direction is supported; and slip occurs at a lower shear stress. The phenomenon has been recognized on many polycrystalline face-centred (f.c.c.) and body-centred (b.c.c.) cubic metals and is apparently most pronounced in systems containing hard second phases; for reviews see [2-5]. Information about the behaviour of intermetallic alloys upon strain reversal is rare. In TiAl alloys the existence of a Bauschinger effect was early suggested by Nakano et al. [6] and Gloanec et al. [7] from the shape of stress-strain hysteresis loops that developed during room temperature fatigue. However, this conclusion was not established quantitatively by comparing the flow stresses in the forward and reverse straining directions. From a fundamental point of view, knowledge of the Bauschinger effect in TiAl alloys is a necessary prerequisite for understanding the materials behaviour in cyclic straining and to develop refined plasticity theories [8]. The loss of strength upon strain reversal is of practical importance because it could be detrimental for the dimensional stability of a load-bearing assembly, when its components are subjected to reverse strain path changes. In the present paper, the Bauschinger effect was studied on a modern high-strength titanium aluminide alloy based on γ(TiAl). Alloys of this type are multiphase assemblies involving several intermetallic phases with different elastic and plastic properties [9, 10]. Deformation of these alloys is naturally very inhomogeneous, which could give rise to the formation of directional internal stresses and yield anisotropy upon load reversal.

2. Experimental investigations

2.1 Alloy composition and microstructure

The alloy investigated (designated TNB-V2) has the composition (at. %) Ti-45.6Al-7.7Nb-0.2C. The alloy was produced by triple vacuum arc re-melting and consolidated by canned hot extrusion at 1230°C with a cross sectional reduction of 6:1. Cylindrical sections of the extrusion (90 mm diameter and 65 mm in length) were annealed at 1310 °C for 30 min, followed by air cooling and a 6 hour stress relief annealing at 800 °C. This heat-treatment produced a nearly lamellar microstructure with about 60 % lamellar colonies [10]. The constitution involves the phases γ(TiAl), α_2(Ti_3Al), β/B2**,** and an orthorhombic phase (oP4) with B19 structure. The B19 structure can be described as having a superstructure of the $D0_{19}$ structure of α_2(Ti_3Al) [11, 12]. The microstructure displayed a banded morphology elongated parallel to the extrusion direction. Texture measurements were not made on this material as a part of this study. However, a previous investigation on similar material processed in the same manner revealed a weak <111> fiber texture of γ grains parallel to the extrusion direction with a maximum intensity of 2 x random [13]. Throughout the text, this material state is designated as “as-received”. It should be mentioned that the fine structural details of the TNB-V2 alloy are very sensitive to the cooling rate after high-temperature annealing. Fast cooling reduces particularly the lamellar spacing and increases the critical flow stress. In the present study, cooling of the extrusion sections was relatively slow due to their large volume. Thus, the critical yield stress of the TNB-V2 variant used in the present investigation is about 150 MPa lower than that of another TNB-V2 variant investigated in a previous study [14].

2.2 Transmission electron microscope (TEM) characterisation

TEM samples were prepared from 0.5 mm thick slices that were cut perpendicularly to the tensile axis. The slices were mechanically ground from both sides to a thickness of 150 μm and then electrolytically polished to electron transparency. The microstructures were examined in the CM 200 and Titan electron microscopes utilizing bright field, weak-beam dark field and high-resolution techniques.

2.3 Mechanical tests

Bauschinger tests have been conducted in many different ways; however, specimen geometry is always a concern in ensuring the validity of the data. Depending on the aspect ratio of the specimen, barrelling or buckling instabilities may occur in the compression segment of the test. Thus, scatter of the results is endemic to Bauschinger studies and arises as much from testing reasons as from variability between specimens. Owing to these geometrical constraints, true tension/compression tests are generally limited to small plastic strains. However, the intention of the present study was to probe the reversal of relatively large strains that are relevant for low cycle fatigue (LCF). This was realized by comparing the deformation behaviour of specimens oriented for forward and backward glide, respectively, under exactly the same conditions. For convenience, the two segments of the Bauschinger test are illustrated in Fig. 1.

In a first step, tensile specimens with a gauge length of 24.5 mm and a diameter of 3.5 mm were machined from the as-received material with the long axis parallel to the extrusion direction. These specimens were deformed at room temperature in a strain-controlled closed-loop machine MTS 810 (MTS System Cooperation). The sample deformation was monitored by an extensometer attached over a 21 mm length of the gauge, which was used as a feed-back parameter. This segment of the Bauschinger test is designated as forward flow.

In the second segment of the test, compression cylinders of 55 mm diameter and 58 mm length and the long axis parallel to the extrusion direction were cut from the as-received material by spark erosion and machining. The end faces of these cylinders were mechanically ground to be flat and parallel with a 20 μm surface finish prior to testing. These cylinders were then compressed between polished hardened steel blocks lubricated with molybdenum disulfide in order to minimize barreling. These tests were performed at room temperature under displacement control in a servo-hydraulic four column machine (Schenck) with a load capacity of 400 t. The specimens were compressed to pre-specified plastic strains of ε_c = 0.5, 1, and 2 %, respectively. True plastic compression was determined from the hydraulic ram displacements by subtracting the elastic deformations of the machine and the sample. Oversized blanks were cut from the compressed cylinders by spark erosion and machined into tensile specimens. These pre-compressed specimens were then tensile tested under the same conditions as described for the as-received material, i.e., the sample dimensions and the deformation machine were the same. During these tensile tests, the deformation direction in the specimens is reversed with respect to that during the compression; thus this segment of the Bauschinger test is designated as reversed flow. This deformation sequence has the advantage that both the forward and reverse segments of the Bauschinger cycle are in tension, i.e., they are not affected by non-axial deformation, buckling or specimen end constraint. Thus, deviation from elastic behaviour upon strain reversal can easily be detected.

A nominal strain rate of $\dot{\varepsilon}_1$ =2.38 x10^{-5} s^{-1} was used throughout the compression/tension loading program. The strain rate sensitivity $(\Delta\sigma / \Delta \ln \dot{\varepsilon})_T$ of the material was measured in the different test segments by performing reversible strain rate changes between $\dot{\varepsilon}_1$ and $\dot{\varepsilon}_2 = 20\,\dot{\varepsilon}_1$. The quantity $\Delta\sigma$ is the difference between the flow stresses σ_1 and σ_2 related to the strain rates $\dot{\varepsilon}_1$ and $\dot{\varepsilon}_2$, respectively, and $\Delta \ln \dot{\varepsilon} = \ln(\dot{\varepsilon}_2 / \dot{\varepsilon}_1)$. Values of load, strain and machine

displacement were continuously recorded at a rate of 100 Hz with 16 bit A/D resolution, utilizing the MTS TESTWARE software.

3. Results and Discussion

3.1 Yield phenomena upon reverse loading

The room temperature strength properties of the as-received material are illustrated in Fig. 2 by stress/strain curves recorded during tensile and compression tests. The critical flow stress and the strain hardening coefficient measured in tension are slightly lower than those measured in compression. Common to both unidirectional compression and tension is, in particular, the plateau in the flow curve, which suggests that forward glide begins relatively abruptly. These observations also suggest that deformation and strain hardening during pre-compression were not significantly affected by barrelling instabilities and friction at the contact surfaces between the machine compression plates and the specimen end faces, as might be expected for the compact pre-compression cylinders. It should also be noted that the uni-directional reference tensile tests are quite reproducible from specimen to specimen, and that the apparent elastic modulus determined from the elastic portion agrees well with the room temperature Young's modulus of γ(TiAl) of E=173 GPa) [15]. Under compression, the average critical flow stress is σ_o=875 MPa and the strain hardening coefficient (determined at 1.5% pre-compression) is $\vartheta = d\sigma / d\varepsilon$ =6576 MPa or ϑ / μ =0.87; μ is the shear modulus [15].

Figure 3 demonstrates the flow curves of the tensile specimens taken from the pre-compressed cylinders (Fig. 1d), representing reversed flow after pre-compression to ε_c=0.5, 1 and 2 %, respectively. The stresses are plotted against the accumulated absolute strain $\varepsilon_a=\varepsilon_c+\varepsilon_r$, comprised of the pre-compression strain ε_c and the tensile strain ε_r measured after strain reversal. For comparison, the tensile curves of the reference material (Fig. 2a) are also plotted

alongside. The characteristic feature of the reversed flow tests is the roundness of the registration curve, i.e., the extended elasto-plastic transient behaviour. The effect increases with increasing pre-compression ε_c. Deviation from Hooke's law (represented by the grey line) seemingly always occurs at a transition stress σ_T of about 127 MPa, i.e., reversed flow starts almost at the outset of reloading, making the identification of a distinct critical flow stress almost impossible. Thus, the reversed flow was described by the stresses (proof stresses) observed at reverse plastic offset strains of ε_r=0.1, 0.2, 0.5, and 1 %, respectively. This data is summarized in Table 1, together with the failure stresses and strains. The Student's *t*-statistical test of this data [16] has demonstrated that in most cases the differences between the offset stresses for forward and reversed deformation were 'highly significant' in statistical terms. For example, a value of t=8.8 was calculated for the $\sigma_{0.5}$ yield stresses measured on the received material (forward flow, ε_c=0) and the specimens tested after 1 % pre-compression. This indicates a very low probability (p<0.01) of the data belonging to the same population. In Table 1 such data is marked with (**). It is notable that a significant increase of the plastic tensile elongation of about 0.3 % after 2% pre-compression was confirmed by the Student's *t*-test. The data designated with (*) is significantly different to that of the received material with p<0.05 or p<0.1, respectively. The remaining data indicated by ($^{\#}$) was not significantly different. The differences in the data for ε_c =0.5, 1 and 2 % are significant (*), except for the difference between the failure strains at ε_c =0.5 and 1 %.

In Bauschinger effect studies mention is often made of permanent softening [3-5, 17]; this is conventionally determined from a plot of the forward and reverse stress/strain curves in terms of absolute stress and absolute (accumulated) strain, $\varepsilon_a=\varepsilon_c+\varepsilon_r$, as shown in Fig. 3. True permanent softening is then defined as a permanent difference between the continued forward flow curve and the inverted reverse flow curve. This definition requires that the two curves

become parallel. In the present study, this was clearly not the case. While the reversed tensile curves become increasingly non-linear with increasing pre-compression ε_c, they do not

Table 1: Experimental data describing transient softening upon strain reversal. ε_c - plastic pre-compression; $\sigma_{0.1}$, $\sigma_{0.2}$, $\sigma_{0.5}$, $\sigma_{1.0}$ - stresses determined at reversed plastic offset strains of ε_r=0.1, 0.2, 0.5, and 1.0 %, respectively; *S* - standard deviation. Data differs very significantly (**), significantly (*) and not significantly ($^{\#}$), from that measured for forward flow (ε_c=0); see accompanying text.

ε_c (%)	*n*	$\sigma_{0.1}$ (MPa) *S* (MPa)	$\sigma_{0.2}$ *(MPa)* *S* (MPa)	$\sigma_{0.5}$ (MPa) *S* (MPa)	$\sigma_{1.0}$ (MPa) *S* (MPa)	σ_f (MPa) *S* (MPa)	ε_r (%) *S* (%)
0	7	769 9.5	772 7.2	796 7.6	838 6.8	860 23.9	1.6 0.1
0.5	10	325** 20	451** 28	718** 37	836$^{\#}$ 16	885** 10	1.7* 0.1
1	14	285** 45	384** 43	589** 62	809$^{\#}$ 72	917** 45	1.7$^{\#}$ 0.3
2	18	249** 7	329** 11	485** 22	642** 37	813* 48	1.9** 0.2

become truly parallel to those of the uni-directional tensile curves representing forward glide. Instead, the envelope of the failure stresses observed after strain reversal is almost a continuation of the forward yield curves. In fact, the reverse flow curves after 1 % pre-

compression are in some cases above those of the forward stress/strain curves. The yield curves measured after 2 % pre-compression seem to suggest a slight softening effect. However, the deformation is still in the elasto-plastic stage, as indicated by the high hardening rate. Thus, the Bauschinger effect in the TiAl alloy investigated is mainly manifested by a loss of a distinct transition between the elastic and plastic deformation regimes often termed as transient softening [18, 19].

3.2 Origin of transient softening

3.2.1 Directional back stresses

As the Bauschinger effect is commonly associated with back stresses produced during forward deformation, it is pertinent at this point to comment on potential sources of such stresses. In an early study Heyn [20] suggested that internal stresses could be produced by inhomogeneous deformation due to “zones of different yield strength” in the material. Thus, after unloading residual stresses arise, which are responsible for the yield lowering effect upon load reversal. This early attempt to explain the Bauschinger effect was strongly supported by tension/compression tests on brass carried out by Masing [21]. For TiAl alloys it has been shown that significant internal stresses develop during monotonic room temperature tensile deformation [14]. The internal stresses were determined by the dip technique on various TiAl alloys with different constitutions and microstructures and a correspondingly wide variation of strength properties. The internal stress, designated σ_μ, was generally very high and could be described as σ_μ=0.8σ. The quantity σ is the yield stress of the alloy at 1% tensile strain; thus, internal stresses of this magnitude are probably relevant for the forward deformation in the Bauschinger tests performed in the present study. Specifically, for the alloy investigated the internal stress was estimated to be σ_μ=640 MPa.

Transmission electron microscope (TEM) examination performed after room temperature deformation has shown that the major deformation mechanisms are glide of $1/2<1\bar{1}0]$ ordinary dislocations and mechanical twinning [22]. With regard to the present study, the point to note is that the dislocations are evenly distributed, with the occasional formation of dislocation multipoles on parallel slip planes. An estimation of the internal stress based on the dislocation density measured after 3 % compression has shown that long-range dislocation interactions contribute to only about 10 % of the internal stress determined by dip testing [14]. Dislocation pile ups, which may concentrate the stress, were seldom observed. Also, de-twinning upon load-reversal is highly unlikely to occur. Thus, the conventional explanation that dislocation structures with directional stress fields cause the Bauschinger effect may not be applicable for the effects observed.

Probably more important for the observed transient softening in TiAl alloys is the inhomogeneous nature of deformation, a point that was early recognized by Mecking et al. [23] and later confirmed by finite element simulations [24- 26]. The intermetallic constituents of the alloy exhibit significant plastic anisotropies mainly due to the lack of independent slip systems that, in terms of the von Mises condition [27], can operate at comparable stresses. A manifestation of this situation in the γ phase is the predominance of $1/2<1\bar{1}0]$ ordinary dislocations. These dislocations provide four slip systems, however, only three of these are independent [28]. Similarly, the α_2 phase exhibits a strong preference for prismatic slip via dislocations with $1/3<11\bar{2}0>$ Burgers vectors; deformation with <**c**> component shear vectors is virtually impossible [29].

Furthermore, in lamellar colonies slip is highly constrained due to the fine scale of the lamellae and the high density of phase interfaces, giving rise to a strong morphological anisotropy [30]. Figure 4 illustrates these aspects for the alloy investigated. The lamellar

morphology shown in (Fig. 4a) is comprised of B19 and γ platelets with the common interface [12]

$$(100)_{B19} \,||\, (111)_{\gamma} \text{ and } [010]_{B19} \,||\, \langle 110 \rangle_{\gamma}. \quad (1)$$

The γ lamellae are interspersed by domain boundaries, which join the orientation variants of γ γ_1 and γ_2. Figure 4b shows one of the domain boundaries (arrowed) in higher magnification. The domain boundary corresponds to a 120° rotational fault between γ_1 and γ_2, meaning, the two γ variants are rotated against each other by 120° around a common $\langle 111 \rangle_{\gamma}$ axis. However, in contrast to the lamellar interfaces, the habit plane of the domain boundary is usually not $\{111\}_{\gamma}$. The misfit between the variants γ_1 and γ_2 is determined by the tetragonality of the γ phase, which amounts to 1-2 %. Such large misfit is usually accommodated by dense structures of misfit compensating defects [9, 22]; which in the present case could not be recognized. This suggests that the misfit was elastically taken up, i.e., the adjacent constituents were uniformly strained to bring the atomic spacings into registry. Such homogeneous misfit accommodation naturally generates high constraint stresses and is only possible if the size of the adjacent constituents is very small, as in the present case.

The disparity between the mechanical properties of the constituents certainly leads to unequal partitioning of stress and strain. In the elastic deformation regime, the load is mainly supported by those grains whose orientations ensure that they are elastically stiff. Once slip has been initiated in favourably oriented grains, further deformation in these grains is accommodated plastically. At this point, a greater proportion of the applied load will be partitioned to those grains that have not yet yielded. Thus, internal back stresses σ_{μ} are formed, which resist forward loading.

A striking feature of the present study is the recognition that this internal stress level is large enough to initiate reverse (compressive) flow when the applied stress remains tensile. This becomes evident by the material response upon unloading from the work hardening region, as demonstrated in Fig. 5. After initial tensile straining, the specimen was repeatedly unloaded to different stresses; the lowest stress was σ_l= 100 MPa and was sufficient to hold the specimen tightly within the grips. The unloading curve shown in Fig. 6a is not exactly linear and parallel to the elastic portion of the curve but exhibits significant roundness in its lower part. Thus, the material begins to yield in the reverse direction well before zero load is reached. In cycle #24, the strain produced by the backward flow is about $\Delta\varepsilon_u$=10^{-3}. When unloading is stopped at the lowest stresses, anomalous anelastic relaxation occurs, i.e., the specimen deforms in the compression direction, and the stress increases with time (Fig. 6b). The total sample elongation ε measured over the same time interval is fairly constant, a pre-requisite for strain controlled relaxation (Fig. 6c) [14]. Upon reloading, the curve bends above the unloading curve as the stress approaches the original value of stress from which it was unloaded. Then, with a little additional plastic strain, the reloading curve becomes a continuation of the main curve as if the unloading had not taken place (Figs. 5, 6a). Thus, dislocation pinning has seemingly not occurred during unloading and relaxation. The observed material response obviously reflects the polarized character of the internal stresses, and that the share of the elastic strains between the constituents is very sensitive to the applied load. Thus, while backward yielding is naturally very limited, it could dramatically change, or even invert, the internal stress pattern. This is a consequence of the large strain misfit produced during the elasto-plastic co-deformation and the high elastic moduli of the intermetallic constituents. It should be noted that similar observations were made during monotonic compression of TiAl alloys; however, the results are less clear because of the unavoidable specimen end constraints.

Based on these considerations, the following scenario is anticipated for the Bauschinger test performed in the present study. In the compression segment of the test, the weak grains of the polycrystalline compound are elastically plus plastically deformed, whereas the hard grains are only elastically deformed. At this point, the two grain families are elastically in a state of compression. Subsequent release of the compressive load gives rise to elastic sample spring back. However, full elastic expansion of the hard grains is hindered by the plastically deformed weak grains. Thus, unloading after initial compression sets the softer grains under residual tension, whereas the hard grains remain under residual compression. This is a good precondition for the tensile segment (backward flow) of the Bauschinger test because the residual stress in the soft grains acts in the same direction as the applied tensile stress.

In this context it is worthwhile to discuss the X-ray studies of Riemer et al. [31] who provided a convincing demonstration of fluctuating internal stresses in polysynthetically twinned (PST) crystals. A PST crystal consists of a single set of γ(TiAl) and α_2(Ti_3Al) lamellae, which enables one to defined the orientation of the lamellar planes with respect to the deformation axis. The residual stresses remaining after room temperature plastic compression were found to depend on the orientation of the deformation axis. While the effects for the so-called *A* orientation with the lamellar planes parallel to the deformation axis can directly be rationalized using the above reasoning, the situation is apparently more complex when the deformation direction is perpendicular to the lamellae interfaces. In this so-called *N* orientation, the α_2 phase is loaded along its c axis and plastically not deformable, because pyramidal slip would be required. However, after compression, residual tensile stresses were recognized in the α_2 phase, which were compensated by compressive stresses in the γ phase. In the framework of the model developed this may be explained as follows. The γ lamellae are comprised of hard and soft domains and hence deform inhomogeneously giving rise to an overall wavy morphology. Thus, an α_2 lamella sandwiched between two γ lamellae has to adapt to this local deformation environment by local bending, which increases its length and

finally sets it under tension. Due to this local bending, limited plastic shear could be elastically transferred though the α_2 lamella. It might be expected that this elastically mediated strain transfer through the α_2 lamellae is only possible if they are very thin.

3.2.2 Dislocation sources and energy dissipation

Another factor supporting transient softening is certainly the presence of fresh dislocations that were produced during forward flow and that in principle are capable in carrying backward deformation. After room temperature compression, comparable to that applied in the present study, the dislocation density is typically 10^7-10^8 cm^{-2} [22]. There is also a high density of elongated dislocation dipoles and prismatic loops (debris), which under the reversed stress may disintegrate or operate as dislocation sources [22]. Thus, with the onset of backward glide sufficient mobile dislocations are available. This is unlike to the situation during uni-directional forward deformation, where, for the onset of glide, an avalanche of new dislocations must be generated.

For backward glide to take place, the glide resistance must be overcome, which requires a more detailed consideration. The TEM evidence is that isolated ordinary dislocations are roughly aligned along their screw orientation and bowed out between jogs [22, 32]. This, together with the fact that the origin of a dipole is often traceable back to ordinary dislocations suggests that the above mentioned dipole defects were trailed and terminated at jogged screw dislocations. Jogs in ordinary screw dislocations can easily form by cross slip because these dislocations have a compact core, and a number of low-index cross slip planes is available [33]. It might be expected that cross slip is triggered by internal stresses. The dislocation slip path associated with un-bowing into the geometrically shortest configuration is about 50 to 100 b [22, 32]. The strain increment associated with this process can be estimated with the help of the Orowan equation. With a dislocation density of $10^8/cm^2$, a strain increment of only 10^{-5} is expected for simple un-bowing. This value is two orders of

magnitude smaller than the unloading increment $\Delta\varepsilon_u$ usually observed after nearly full unloading (Fig. 6a). Although this estimation is crude, it shows that during unloading significant dislocation backward motion occurs, which is obviously supported by the back stresses.

A salient feature of the dislocation fine structure is that the dislocations in the stress-free TEM foil remained bowed out in a smooth arc between the jogs. This finding indicates that lattice friction forces occur on all dislocation characters and impede a complete relaxation of the bowed segments into the geometrically shortest configuration between the obstacles.

The friction stress arises as a direct consequence of the lattice periodicity; the relevant structural unit, the kink, has atomic dimensions. Atomistic calculations by Simmons et al. [34] revealed a high friction arising from a Peierls-type mechanism, particularly along the screw and 60° mixed ordinary dislocation directions. Due to its atomic nature, the friction stress can reverse its sign within the length scale of lattice periodicity.

At the beginning of reloading, the lattice friction that stabilized the dislocations in a bowed out configuration must be overcome. It might be speculated that the resulting friction stress part is manifested as the relatively low transition stress σ_T=127 MPa between pure elastic and elasto-plastic deformation (Fig. 3). As already mentioned in Sect. 3.1, σ_T is almost independent of the amount of pre-compression. However, the forward and backward motion of a screw dislocation is not fully reversible. This is because a jog can conservatively glide along a screw dislocation. Thus, on the same dislocation, the distribution of the jogs may be different during it's to- and fro-glide. Then, during its backward motion, the dislocation has to intersect the debris and dipoles previously left in its wake. Furthermore, a vacancy-producing jog has to produce interstitials if it moves in the opposite direction. These factors may cause further cross slip and debris to be produced, which would explain the higher hardening rate of the reloading curve in the elasto-plastic regime.

This difference in glide resistance for forward and backward motion of the dislocations probably gives rise to the mechanical hysteresis within an unloading/reloading cycle (Figs. 5, 6a), often taken as a signature of energy dissipation. The area within the hysteresis loop is the energy per unit volume Q_H dissipated by dislocation glide, usually in the form of heating. Following the arguments given above, it is expected that the hysteresis energy is primarily determined by the extent of backward flow. Thus, Q_e should increase with increasing unloading stress increment $\Delta\sigma_u$. Likewise, Q_e should increase with strain ε (or work hardening) because then higher back stresses are generated, which drive backward flow. Figure 7 demonstrates these two effects, giving supporting evidence for this interpretation. Basically the same dissipation process, even though exacerbated, is expected when the specimen is subjected to the full compression/tension cycle. Thus, although the work hardening rates in the two segments of the Bauschinger test are quite different (Fig. 3), the same dislocation glide resistance should be present in these segments. In the present study, the dislocation glide resistance was assessed by measuring the strain rate sensitivity, as described in Sect. 2.3. The stress increment $(\Delta\sigma / \Delta \ln \dot{\varepsilon})_T$ that occurs upon strain rate cycling at constant temperature can be related to the activation volume V of the relevant thermally activated process by [35]

$$V = \frac{M_T kT}{(\Delta\sigma / \Delta \ln \dot{\varepsilon})_T} \tag{2}$$

as described in [9, 20]. The quantity $M_T = 3.06$ is the Taylor factor. Figure 8 shows the stress/strain curves of as received (forward glide) and pre-compressed (backward glide) specimens involving reversible strain rate cycles. The evaluation in terms of eq. (1) yields the data that is summarized in Fig. 9, together with the evolution of the work hardening coefficient $\vartheta = d\sigma / d\varepsilon$, normalized by the shear modulus μ of the material [15]. Accordingly,

the activation volume is not affected by the pre-deformation, meaning, the glide resistance is the same for forward and backward glide of the dislocations. The average value is V=1.4x10^{-18} mm^3 or V=65 b^3, when referred to the Burgers vector of the ordinary dislocations. A detailed discussion in [9, 22] has shown that this value is consistent with a glide resistance resulting from a combination of jog dragging and lattice friction.

4. Conclusions

The Bauschinger effect in a multiphase titanium aluminide alloy based on γ(TiAl) is manifested by the loss of a distinct transition between elastic to plastic deformation. However, there is no permanent softening in the backward segment of the test.

This transition softening is attributable to heterogeneous deformation of the multiphase microstructure in the forward segment of the test, which produces directional internal back stresses.

The internal stress pattern impeding forward deformation is largely inverted upon unloading from initial forward glide and hence supports deformation after strain reversal.

Another factor supporting deformation in the reversed direction is the presence of fresh dislocations and the availability of dislocations sources that were produced during forward glide. This reduces the requirement to activate new dislocation sources.

Taken together, these factors lead to a softer reverse response and a smooth transition between the elastic and elastic-plastic regimes in the reverse stress-strain curves.

The experimental approach taken in the present study has been macroscopic. Details of the mechanisms certainly occur at the dislocation level; this remains a fruitful area for electron microscope studies.

Acknowledgements

The authors gratefully acknowledge the financial support provided by the German Science Foundation (DFG) via Projects AP/49-5 and AP/49-6. We also thank our colleagues J. Knaack and U. Lorenz for help with compression tests.

References

[1] Bauschinger J. Über die Veränderung der Elastizitätsgrenze und der Festigkeit des Eisens und des Stahls durch Strecken und Quetschen, durch Erwärmen und Abkühlen und durch oftmals wiederholte Beanspruchung. Mitt. Mech.-Tech. Laboratorium K. Technische Hochschule München 1886;13(5):1-115.

[2] Wilson DV. Reversible work hardening in alloys of cubic metals. Acta Metall 1965;13:807-813.

[3] Brown LM, Stobbs WM. The work hardening of copper-silica. I. A model based on internal stresses, with no plastic relaxation. Philos Mag 1971;23:1185-1199.

[4] Brown LM, Stobbs WM. The work hardening of copper-silica. Philos Mag 1971;23:1201-1233.

[5] Embury D J. Plastic flow in dispersion hardened materials. Metall Trans A 1985;16A:2191-2200.

[6] Nakano T, Yasuda HY, Higashitanaka N, Umakoshi Y. Anomalous behaviour of cyclic deformation and fatigue properties of TiAl PST crystals. Acta Mater 1997;45:4807-4821.

[7] Gloanec AL, Jouiad M, Bertheau D, Grange M, Hénaff G. Low-cycle fatigue and deformation substructures in an engineering TiAl alloy. Intermetallics 2007;15:520-531.

[8] Wilson DV, Bate PS. Reversibility in the work hardening of spheroidised steels. Acta Metall 1986;34:1107-1120.

[9] Appel F, Paul JDH, Oehring M. Gamma titanium aluminide alloys – science and technology. Weinheim: Wiley VCH; 2011.

[10] Appel F, Oehring M, Wagner R. Novel design concepts for gamma-based titanium aluminide alloys. Intermetallics 2000;8:1283-1312.

[11] Nguyen-Manh D, Pettifor DG. Origin of O phase and pseudo-twinning in Ti-Al-Nb alloys: a first-principles studies. In: Kim Y-W, Dimiduk DM, Loretto MH, editors. Gamma titanium aluminides 1999. Warrendale PA: TMS; 1999, p. 175-182.

[12] Appel F, Oehring M, Paul JDH. A novel composite structure in TiAl alloys. Mater Sci Eng A 2008;493:232-236.

[13] Brokmeier HG, Oehring M, Lorenz U, Clemens H, Appel F. Neutron diffraction study of texture development during hot working of different gamma titanium aluminide alloys. Metall Mater Trans A 2004;35A:3563-3579.

[14] Hoppe R, Appel F. Deformation-induced internal stresses in multiphase titanium aluminide alloys. Acta Mater 2014;64:169-178.

[15] Schafrik RE. Dynamic elastic moduli of the titanium aluminides. Metall Trans A 1977;8a:1003-1006.

[16] Fisher RA. Statistical methods for research workers, 13th edition. Edinburgh: Oliver and Boyd; 1958.

[17] Atkinson JD, Brown LM, Stobbs WM. The work hardening of copper silica: VI. The Bauschinger effect and plastic relaxation. Philos Mag 1974;30:1247-1280.

[18] Pragnell PB, Stobbs WM, Withers PJ. Consideration in the use of yield asymmetries for the analysis of internal stresses in metal matrix composites. Mater Sci Eng A 1992;159:51-63.

[19] Pragnell PB, Downes T, Withers PJ, Lorentzen T. An examination of the mean stress contribution to the Bauschinger effect by neutron diffraction. Mater Sci Eng A 1995;197:215-221.

[20] Heyn E. A few questions from the field of metal testing. Metall und Erz 1918;15:411-422 and 436-441.

[21] Masing G: Zur Heynschen Theorie der Verfestigung der Metalle durch verborgen elastische Spannungen. Mitteilungen aus dem Forschungslaboratorium Siemensstadt 1923; 3:231–239.

[22] Appel F, Wagner R. Microstructure and deformation of two-phase γ-titanium aluminides. Mater Sci Eng R 1998;22:187-268.

[23] Mecking H, Hartig Ch, Kocks UF, Hartig Ch. Deformation modes in γ-TiAl derived from the single crystal yield surface. Acta Mater 1996;44:1309-1321.

[24] Kad BK, Dao M, Asaro RJ. Numerical simulations of plastic deformation and fracture in two-phase γ-TiAl+$\alpha_2$$Ti_3$Al lamellar microstructures. Philos Mag A 1995;71;567-604.

[25] Schlögl SM, Fischer FD. Numerical simulation of yield loci for PST crystals of TiAl. Mater Sci Eng A 1997;239:790-803.

[26] Brockman RA. Analysis of elastic-plastic deformation in TiAl polycrystals. Int J Plasticity 2003;19:1749-1722.

[27] Von Mises R. Mechanik plastischer Formänderungen von Kristallen. Z Angew Math 1928;8:161-185.

[28] Goo E. Application of the von Mises criterion to single and dual phase TiAl. Scripta Mater 1998;38:1711-1716.

[29] Inui H, Toda Y, Shirai Y, Yamaguchi M. Orientation dependence of fracture behavior of Ti_3Al single crystals. Philos Mag A 1994;69:1161-1169.

[30] Fujiwara T, Nakamura A, Hosomi M, Nishitani SR, Shirai Y, Yamaguchi M. Deformation of polysynthetically twinned crystals of TiAl with a nearly stoichiometric composition. Philos Mag A 1990;61:591-606.

[31] Riemer M, Jentsch HG, Biermann H, Mughrabi H. The internal stress state in lamellar PST-crystals of the intermetallic alloy TiAl after compressive deformation. Intermetallics 1999;7:241-249.

[32] Appel F, Herrmann D, Fischer FD, Svoboda J, Kozeschnik E. The role of vacancies in work hardening and fatigue of TiAl alloys. Int Journal Plasticity 2013;42:83-100.

[33] Jiao Z, Whang SH, Yoo MH, Feng Q. Stability of ordinary dislocations on cross-slip planes in γ-TiAl. Mater Sci Eng A 2002;329-331:171-176.

[34] Simmons JP, Rao SI, Dimiduk DM. Effect of planar fault energies on dislocation core structures and mobilities in $L1_0$ compounds. In: Baker I, Darolia R, Whittenberger JD, Yoo MH, editors. High-Temperature Ordered Intermetallic Alloys V, Materials Research Society Symposia Proceeding, vol. 288. Pittsburgh PA: MRS; 1995, pp. 335-342.

[35] Schoeck G. The activation energy of dislocation movement. Phys Status Solidi 1965;8:495-507.

Figures and Captions

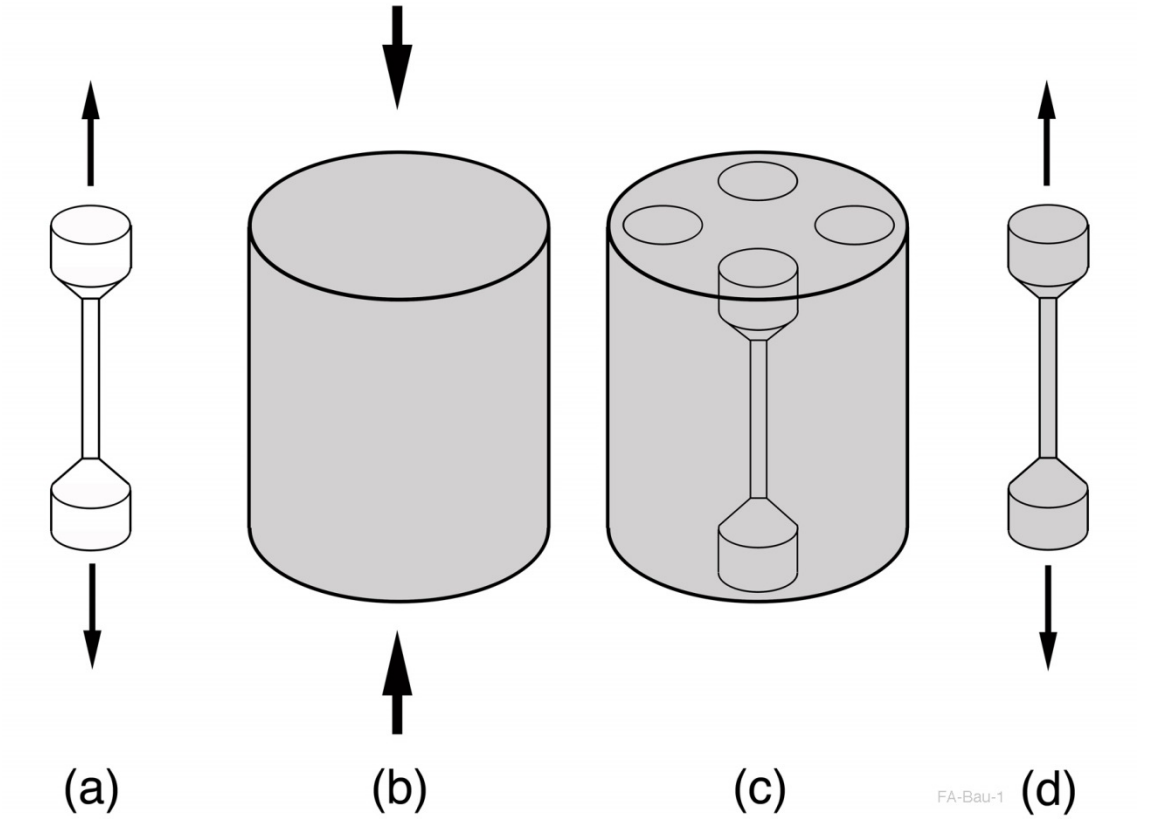

Fig. 1. Schematic illustrating the segments of the Bauschinger test performed in the present study. The extrusion direction is vertical for all the specimen forms shown in Figs. (a) to (d). (a) Tensile test performed on the as-received material representing forward flow. (b) Compression of cylinders to strains ε_c=0.5, 1 and 2%, respectively. (c) Manufacturing of

tensile specimens from compressed material. (d) Tensile test performed on pre-compressed material representing reversed flow.

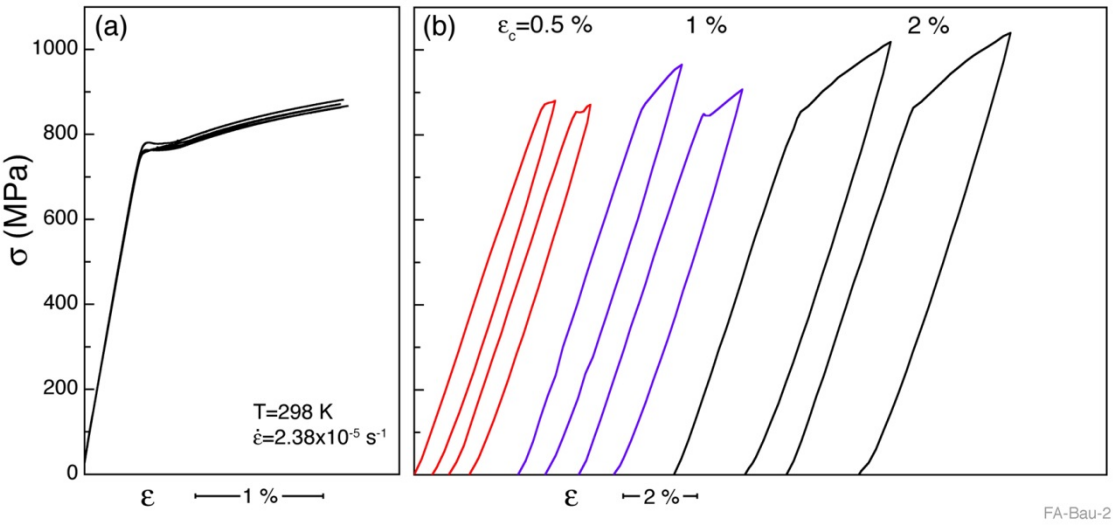

Fig. 2. Mechanical properties of the as-received material at room temperature. (a) Stress (σ) versus strain (ε) curves of tensile tests (Fig.1a). (b) Stress/strain curves of the pre-compression tests (Fig. 1b).

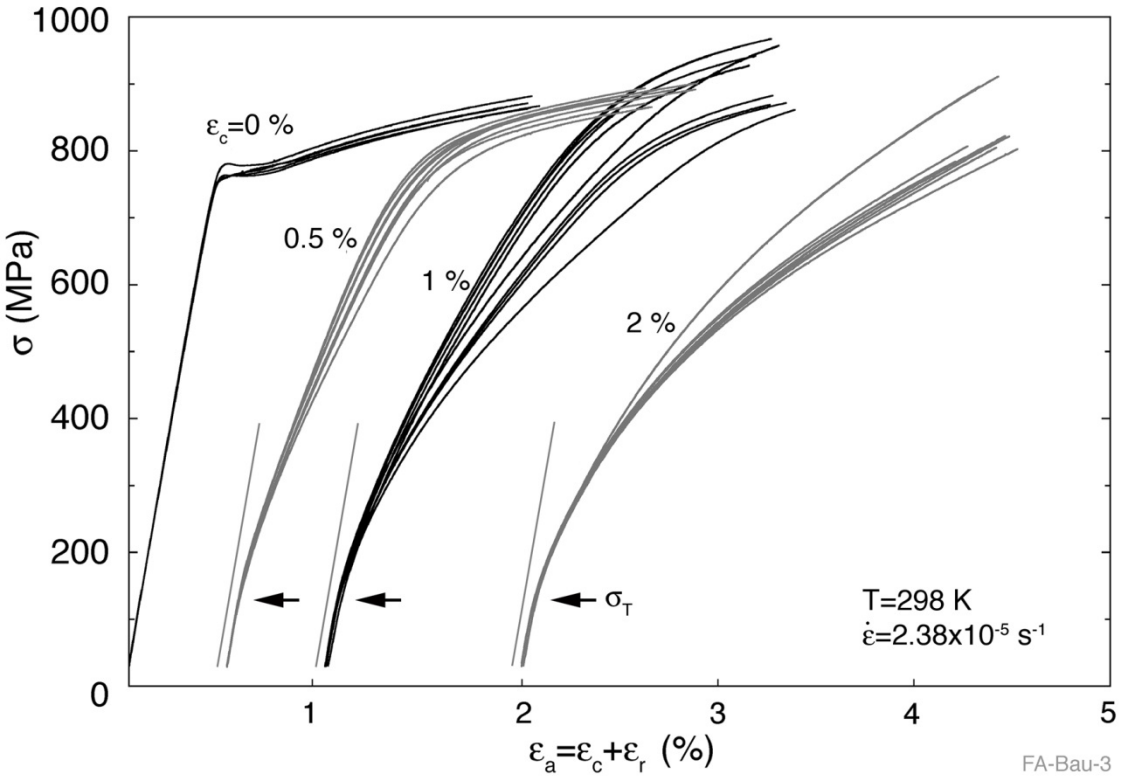

Fig. 3. Stress (σ) versus strain (ε) curves of tensile tests performed on pre-compressed material, with the pre-compression strain ε_c indicated. The stresses are plotted as accumulated absolute strains $\varepsilon_a=\varepsilon_c+\varepsilon_r$, comprised of the pre-compression strain and the tensile strain measured after strain reversal. The stress σ_T=127 MPa designates the transition stress from pure elastic to elasto-plastic deformation. The grey lines represent Hooke's law calculated from the specimen elasticity. For comparison, the tensile curves of the as-received material (ε_c=0 %) are shown.

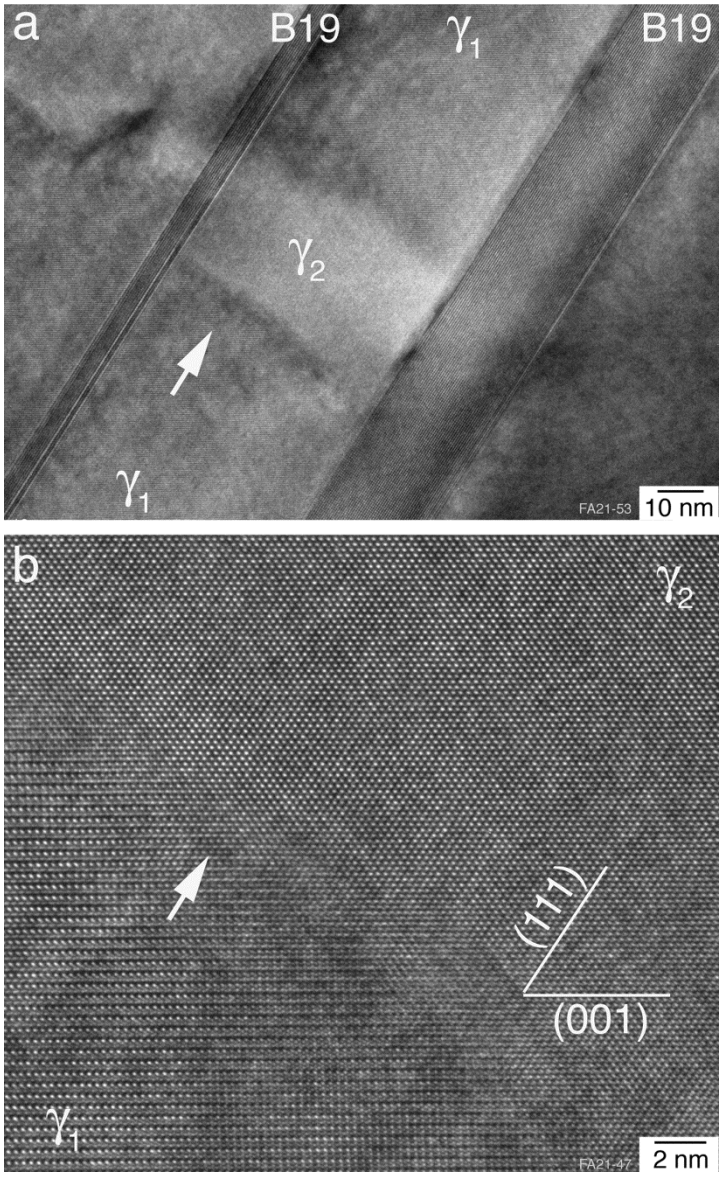
a
B19
γ_1
B19
γ_2
γ_1
FA21-53
10 nm
b
γ_2
(111)
(001)
γ_1
FA21-47
2 nm

Fig. 4. Fine structure of the alloy investigated. (a) Low-magnification, high-resolution micrograph of the lamellar morphology consisting of B19 and γ platelets. The central γ lamella is comprised of the orientation variants γ_1 and γ_2, which are joined by two domain boundaries. (b) Higher magnification of one of the domain boundaries (arrowed). Domain γ_1 is imaged along its $< \bar{1}\,10]$ direction, which reveals the ordering of the $(002)_\gamma$ planes. Domain γ_2 is imaged along $< \bar{1}\,01]$.

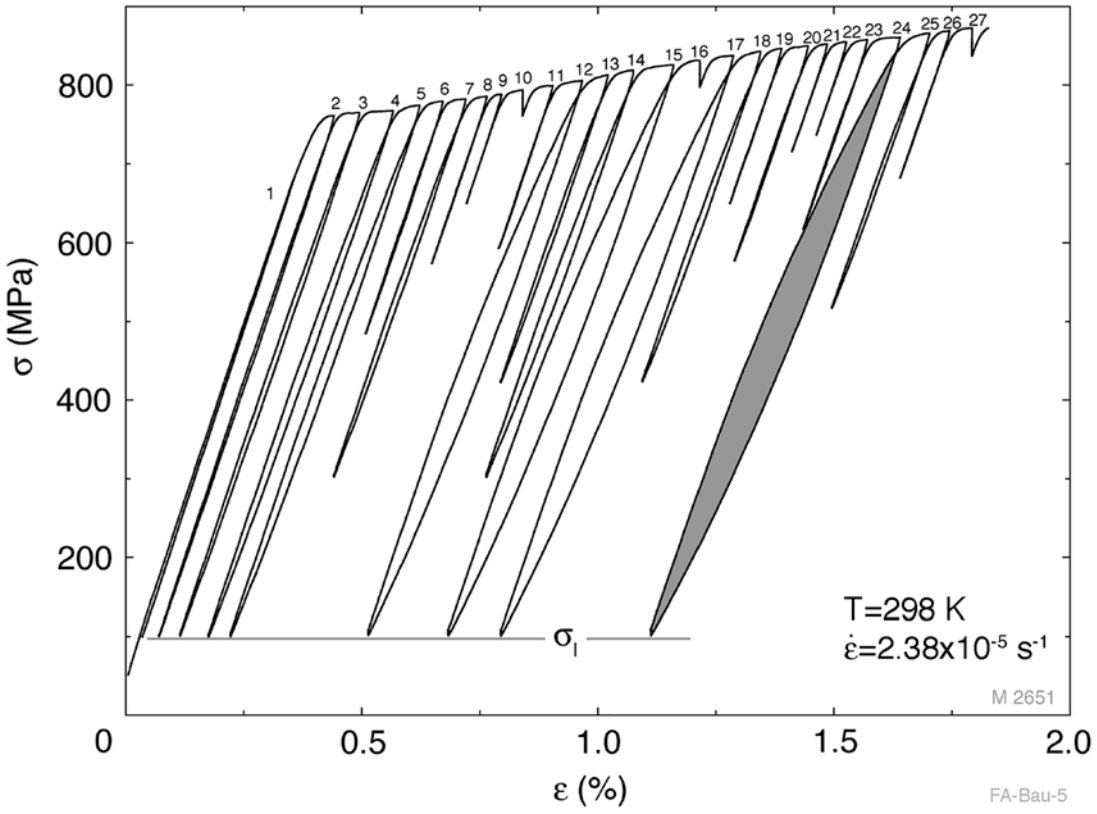

Fig. 5. Pseudo-elastic effects observed during initial tension representing forward flow (Fig.3, ε_c=0 %). In the course of the strain controlled test, unloading/reloading cycles to different lower stresses were performed.

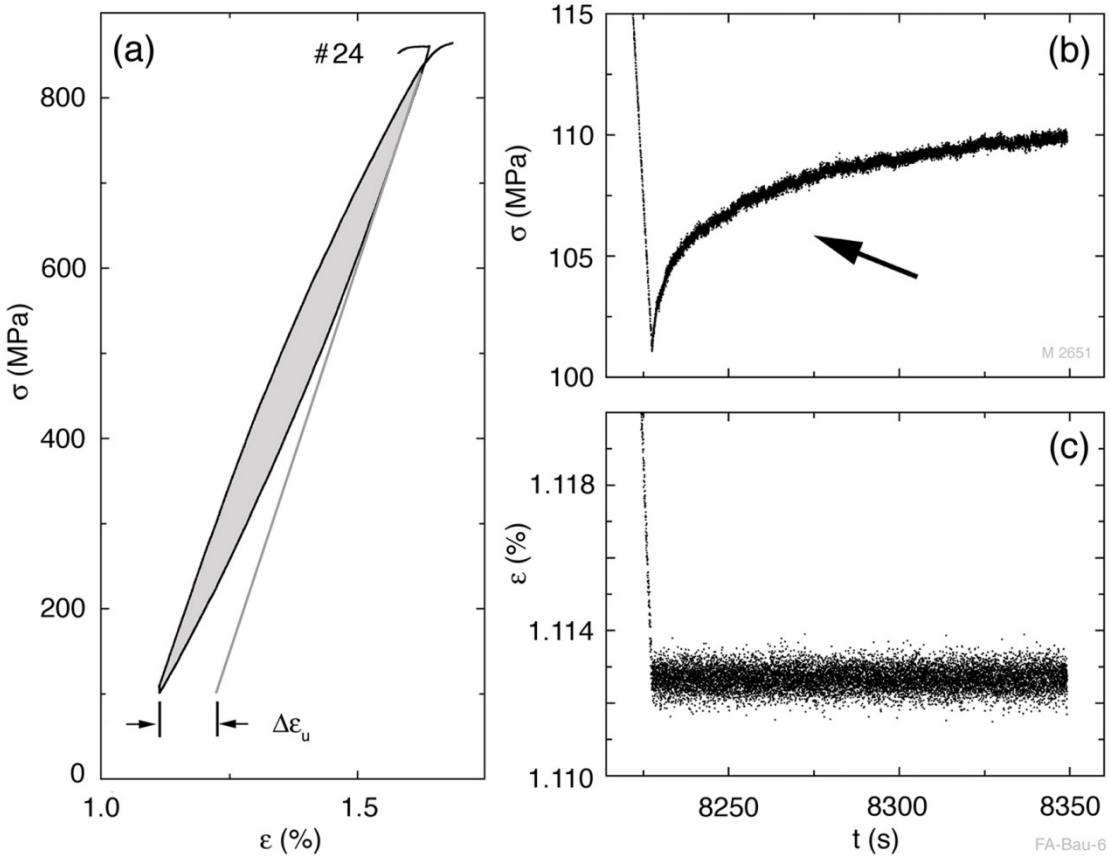

Fig. 6. Unloading response after initial tension. (a) Hysteresis loop formed during the unloading/reloading cycle #24 involved in the tensile test shown in Fig. 5. The grey line represents Hooke's law calculated from the specimen elasticity. (b) Relaxation kinetics

observed after unloading to σ_l= 100 MPa. Note the anomalous increase of the stress σ with time *t*. (c) Total (elastic + plastic) sample elongation ε measured over the same time interval.

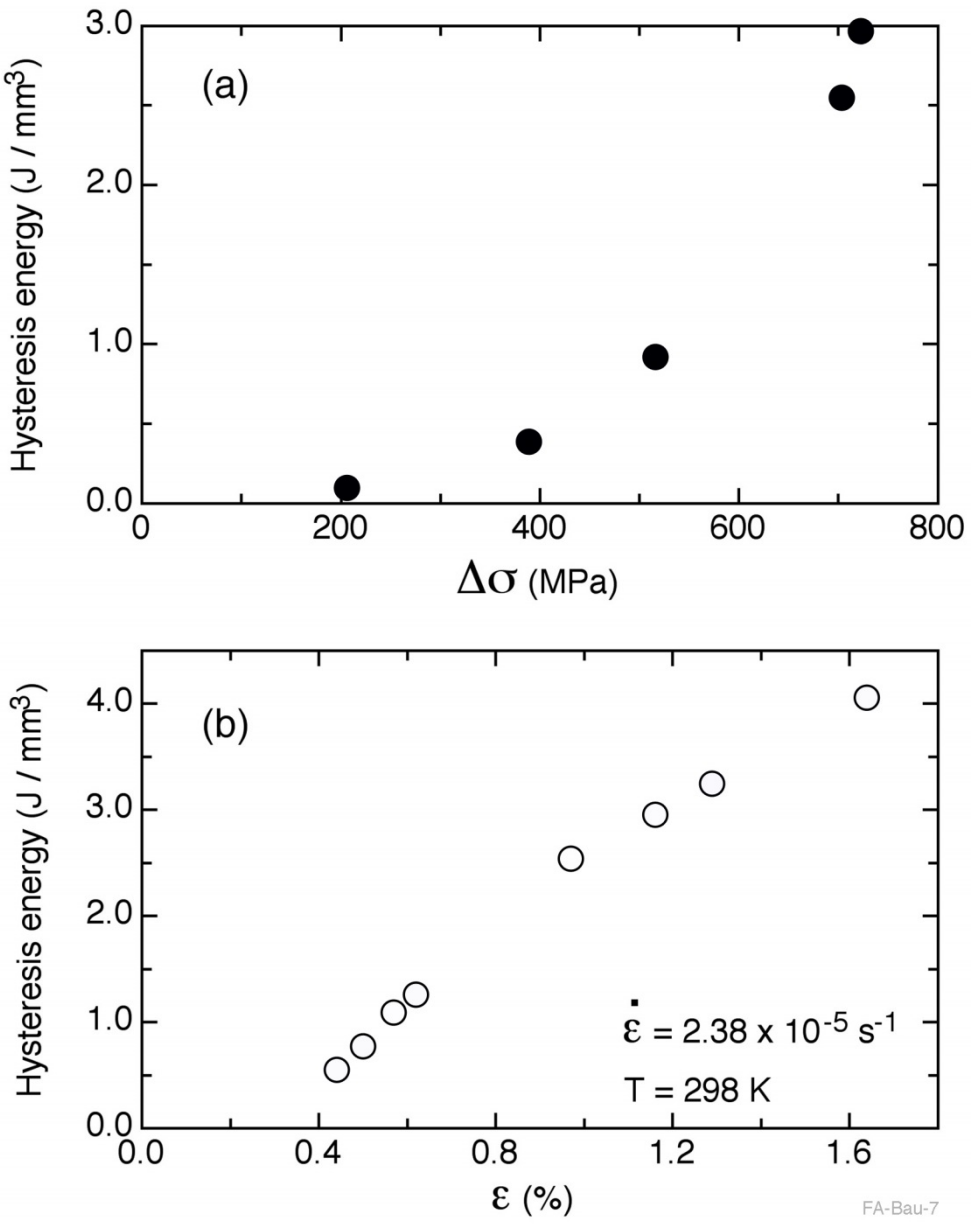

Fig. 7. Energy dissipation during unloading/reloading cycles after initial tension. (a) Dependence on the hysteresis energy Q_H per cycle and unit volume on the unloading stress increment $\Delta\sigma_u$. Evaluation of cycles #11 to 15 in Fig. 4. (b) Dependence of the hysteresis energy Q_H on strain ε. Evaluation of cycles #2-5, 12, 15, 17, 24 in Fig. 4.

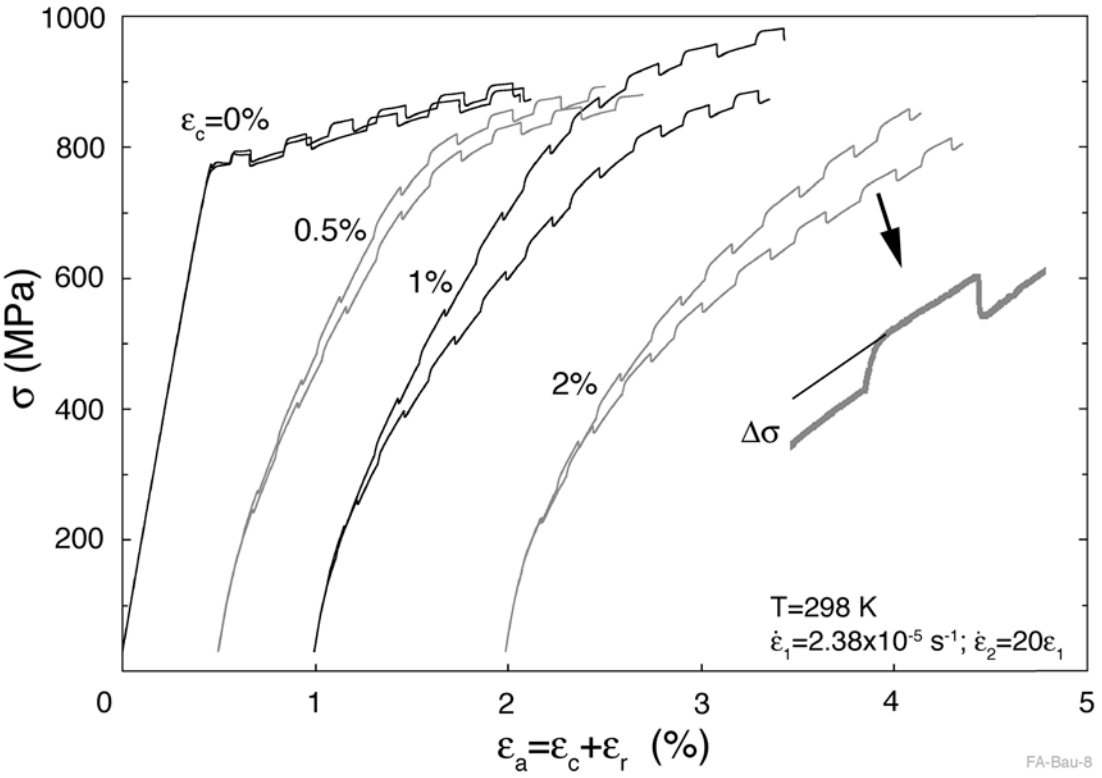

Fig. 8. Stress/strain curves involving reversible strain rate cycling tests performed on as-received (forward glide) and pre-compressed (backward glide) specimens. Strain controlled tensile tests.

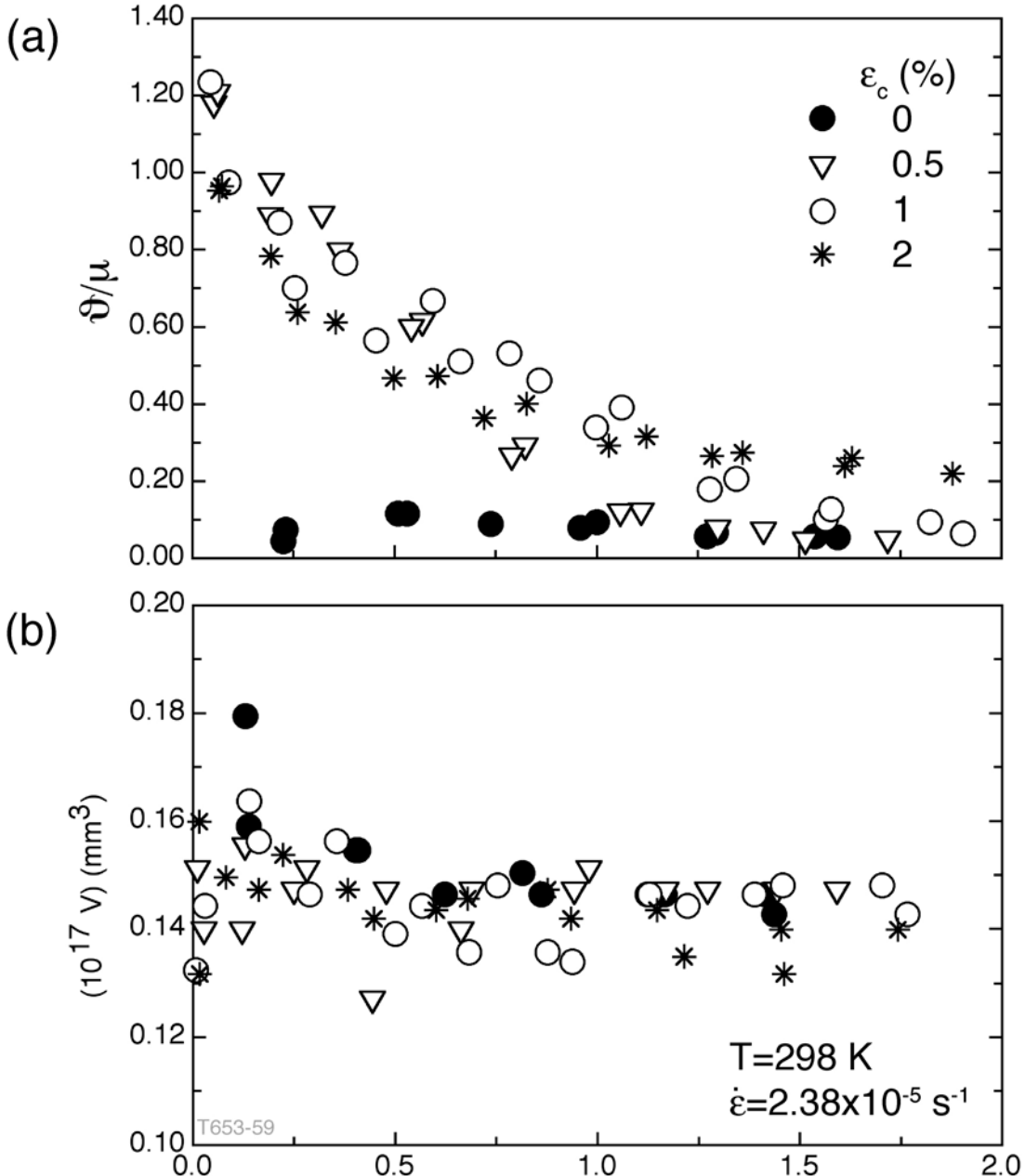
(a)
1.40
1.20
1.00
0.80
0.60
0.40
0.20
0.00
ϑ/μ
εc (%)
0
0.5
1
2
(b)
0.20
0.18
0.16
0.14
0.12
0.10
(10^17 V) (mm^3)
T=298 K
ε̇=2.38x10^-5 s^-1
T653-59
0.0
0.5
1.0
1.5
2.0

Fig. 9. Deformation characteristics of as-received and pre-compressed material. Dependence of (a) the normalized strain hardening coefficient ϑ / μ and (b) the activation volume on strain ε.